ELSEVIER

Contents lists available at ScienceDirect

International Journal of Heat and Mass Transfer

journal homepage: www.elsevier.com/locate/hmt





Impact of conjugate heat transfer on the turbulence and heat transfer in an upward heated pipe flow at supercritical pressure

Jundi He a,*, Wei Wang b, Bing Xu c, Shuisheng He a

- ^a Department of Mechanical Engineering, University of Sheffield, Sheffield, S1 3JD, UK
- ^b Scientific Computing Department, Science and Technology Facilities Council, Daresbury, WA4 4FS, UK
- ^c EDF Energy, Javelin House, Gloucester Business Park, Gloucester, GL3 4AE, UK

ARTICLE INFO

Keywords: Direct numerical simulation Supercritical fluid Conjugate heat transfer Heat transfer deterioration Laminarisation

ABSTRACT

Direct numerical simulations (DNS) of an upward heated pipe flow of supercritical CO₂ (at $Re_0 = 3600$) were carried out with and without conjugate heat transfer (CHT). The aim is to identify the impact of CHT on this specific flow problem and provide information for relevant numerical studies. The configuration is referred to one of the experiments carried out by Luo (2014), with a stainless steel (SS 304) pipe and a thermal activity ratio of 0.061. When CHT is introduced, the predictions of heat transfer coefficient (HTC) and wall temperature obtained in DNS are slightly improved against the experiment measurements. Two primary factors arise when CHT is considered, which are the axial redistribution of wall heat flux and the damping of the enthalpy fluctuations. The former affects the heat transfer particularly within a short distance after the inlet, leading to a more rapid establishment of the thermal boundary layer and a more rapidly progressing 'laminarising' process. The latter introduces substantial differences in the fluctuations of enthalpy (~ 30 times difference) and density (~ 40 times difference), which is however confined within a small region close to the wall and diminishes rapidly further away, resulting in a minor effect on turbulence and heat transfer in the main flow. When CHT is omitted, turbulent kinetic energy is over-predicted up to 1.55 times at most, in particular when the flow is being 'laminarised' (z/D < 30). This is attributed to the discrepancies in shear production rather than the buoyancy production of the turbulent kinetic energy. Additionally, CHT alters both the laminar (Nu_i) and turbulent contributions (Nu_t) to the Nusselt number, with Nu_t starting at a lower level close to the inlet and the peak of Nu_i being reduced by 12.3%. These findings provide an insight on the impact of CHT on turbulence and heat transfer at different stages and valuable information for a more accurate modelling method for supercritical fluid flows.

1. Introduction

For a fluid above its critical pressure, there will be no phase change as the temperature rises, while its thermophysical properties may vary drastically. Such a fluid, which is commonly referred to as a supercritical fluid, is an efficient working fluid used in many engineering systems, such as supercritical water-cooled reactors (SCWR), power generation cycle and geothermal systems. It is well known that heat transfer deterioration occurs in heated upward (or cooled downward) flows at supercritical pressure under the influence of buoyancy. This abnormal heat transfer feature has been extensively investigated in numerous studies [e.g. 1–7]. Research efforts have been dedicated to understand the mechanisms of the heat transfer deterioration accompanied by laminarisation and recovery accompanied by re-transition [8–15]. These studies also explored the effects of flow and thermal conditions (inlet temperature, Reynolds number, wall heat flux, etc.)

and the development/validation of various heat transfer correlations on turbulence and heat transfer.

Most numerical studies on supercritical fluids were carried out by simulating the fluid without explicitly considering the conduction through the solid wall, in which thermal boundary conditions were implemented at the fluid boundary. This idealised and simplified approach generally works well, though under certain circumstances, it may result in significant uncertainties in the prediction. In experiments, the fluid is normally heated by a solid pipe, duct or similar facility, resulting in non-uniform heating due to the heat redistribution via the solid conduction. Such effect becomes more pronounced when there is a significant variation in heat transfer at the axial (such as towards the end of a heated section) or circumferential directions. Pucciarelli and Ambrosini [16] studied this effect using large eddy simulations,

E-mail address: jundi.he@sheffield.ac.uk (J. He).

Corresponding author.

Nomenclature	
Superscripts	
,	fluctuating component of the Reynolds
"	average
	fluctuating component of the Favre average
*	dimensional values
Greek letters	
λ^*	thermal conductivity $(W/(m \cdot K))$
μ^*	dynamic viscosity (Pa · s)
$ u^*$	kinematic viscosity (m ² /s)
$ ho^*$	density (kg/m³)
Roman Letters	
c_p^*	specific heat (J/K)
D^*	diameter (m)
Fr	Froude number $(Fr_0 = u_0^* / \sqrt{g^* R^*})$
g*	gravitational acceleration
h^*	specific enthalpy (J/kg)
K	thermal activity ratio $\sqrt{\rho_f^* \lambda_f^* c_{p,f}^* / \rho_s^* \lambda_s^* c_s^*}$
L^*	streamwise length of domain (m)
Nu	Nusselt number ($Nu = HTC D^*/\lambda^*$)
P*	pressure (Pa)
Pr	Prandtl number $(Pr = c_p^* \mu^* / \lambda^*)$
q_s^*	volumetric heating source (W/m^3) wall heat flux (W/m^2)
q_w^*	radial location
r R*	pipe radius (m)
Re	Reynolds number based on pipe radius
110	$(Re = u^*R^*/v^*)$
T^*	temperature (K)
t^*	time (s)
u^*	velocity (m/s)
y	distance from the wall $(y = 1 - r)$
z	streamwise location
Subscripts	
0	values at the inlet
heta	spanwise location
b	bulk value
f	values for fluid domain
i	index of direction
pc	pseudo-critical state
r	radial direction
S	values for solid domain
w	values at the wall
Z	streamwise direction

investigating supercritical water flows in a rectangular channel with and without conjugate heat transfer (CHT). The flow has a Reynolds number of 3868 (based on pipe diameter) and a wall thickness equals to the half-channel height. Significant differences in wall temperature and turbulent kinetic energy were observed when CHT was implemented. In particular, when the flow is fully-laminarised, the peak of turbulent kinetic energy (TKE) was halved due to the consideration of CHT. Moreover, the fluctuations in temperature close to the wall were significantly dampened due to the presence of the solid wall.

Two effects are introduced when conjugate heat transfer is considered in a numerical simulation: (i) damping of temperature fluctuations, particularly close to the wall and (ii) redistribution of wall heat flux. The damping effect of CHT in DNS was initially studied by Tiselj et al. [17], in which DNSs with CHT at various thermal activity ratios $K = \sqrt{\rho_f^* \lambda_f^* c_{p,f}^* / \rho_s^* \lambda_s^* c_s^*}$ were carried out and compared. In a CHT simulation, the thermal boundary condition is neither Neumann nor Dirichlet condition, but an intermediate condition strongly influenced by the ratio of effusivities (K) [18]. In [17], when K is reduced from infinity (without CHT) to 0.1, root-mean-square of the temperature fluctuations near the wall were found to be dampened by about 9 times. The damping effect on supercritical fluid flow was studied by Nemati et al. [19] through direct numerical simulations (DNS). DNS of two forced convection pipe flows of supercritical CO_2 at $Re_{\tau} = 360$ were carried out with two different thermal boundary conditions: (i) a uniform wall heat flux and (ii) an equivalent wall enthalpy which is constant in time, in which the enthalpy fluctuations at the wall were forced to be zero. The magnitude of viscous diffusion, dissipation and production of turbulent kinetic energy budget terms are all slightly smaller in case ii than in the case i, especially for locations close to the pipe wall. In case ii, in comparison with case i, the laminar and inhomogeneous contributions to the Nusselt number remain largely the same, while turbulent contribution was slightly reduced when the enthalpy fluctuations were dampened. The study quantified the contributions of wall enthalpy fluctuations to heat transfer and turbulence in an example of forced convection, providing comprehensive insights to the damping effect introduced by considering CHT.

In addition to high-fidelity simulations, some numerical studies based on Revnolds-averaged Navier-Stokes (RANS) simulations also considered conjugate heat transfer [20-23]. Zhou and Krishnan [20] simulated supercritical sulfur hexafluoride flows (Re = 650) in a Tshape channel using the low-Reynolds number $k-\epsilon$ (Chien) model [24]. The numerical results were validated against experiments and the peak of wall temperature was found to appear more upstream in experiments. The comparisons on the general trends of horizontal and upward flows were satisfactory against experiments, with the wall temperatures reasonably predicted. Wang et al. [21] studied the effects of solid thermal conductivity by conducting conjugate heat transfer simulations of supercritical cryogenic methane flows in a rectangular cooling channel. The redistribution of the wall heat flux was significantly influenced by the varying thermal conductivity. A new empirical correlation for Nusselt number was as well developed based on the Jackson & Hall [25] correlation. Comparisons between the numerical results of vertical flows of supercritical CO2 in an annular channel based on different turbulence models and experiments were carried out in [22,23]. The examined turbulence models include the AKN [26,27], V2F [28] and YS [29] models, in which the AKN model yields the best agreement with experimental measurements.

CHT is sometimes necessary in order to understand the impact of modifying the pipe wall geometry and it has been widely applied in RANS simulations. For example, [30] conducted CHT RANS simulations of supercritical CO2 flows in a helical coiled tube and observed the periodical variations in wall temperature and heat transfer coefficient. Sun et al. [31] studied the impact of buoyancy with a varying Reynolds number, wall heat flux and pipe diameter in supercritical aviation kerosene (RP-3) flows in a horizontal tube using CHT RANS simulations with the standard $k - \epsilon$ model. The redistribution of wall heat flux between the top and bottom walls was introduced when CHT was considered, and circumferential stratification was observed. The same numerical method was used in another study on supercritical RP-3 flows in a ribbed tube by Xu et al. [32] and enhancement of heat transfer was found at the inlet region due to the presence of the ribs. CHT simulations of developing laminar flows of supercritical CO₂ in multi micro-channels were carried out by Khalesi et al. (2019, 2020), showing significant effects on friction factor and heat transfer coefficient due to the strong change in thermophysical properties.

On one hand, the inclusion of CHT is motivated in the above RANS studies by the fact that the flow problems are linked with the nonnegligible impact of the solid geometry, while on the other hand, CHT in the wall is nearly always omitted in DNS/LES studies, which often focus on understanding the fundamental flow/thermal physics. Out of the two factors of conjugate heat transfer noted earlier, RANS simulations with CHT, only resolve the non-uniform heat distribution in the wall but the effects of the dampened temperature fluctuations are not resolved. The DNS study conducted by Nemati et al. [19] considered the latter only in a forced convection scenario without including the buoyancy effect. A research gap exists in comparing DNS flows with and without conjugate heat transfer to reveal the impact of CHT in the buoyancy-influenced turbulence and heat transfer. In the present study, a supercritical CO2 flow from one of the experiments carried out in [33] is reproduced in DNS, with and without conjugate heat transfer to study the differences between the two simulations and provide useful information on the interpretation of results from the default approach in DNS, i.e. without CHT.

2. Methodology

2.1. Numerical method

Direct numerical simulations in the present study were carried out using the DNS solver CHAPSim [34–36]. CHAPSim was originally a solver for incompressible and isothermal flows but was later extended to solving the thermal flow with strong variations in thermophysical properties with low-Mach-number approximation [37] applied, in which the acoustic interactions and compressibility effects are neglected. The governing equations are written in a cylindrical coordinate:

$$\frac{\partial \rho}{\partial t} + \frac{\partial \left(\rho u_z\right)}{\partial z} + \frac{1}{r} \frac{\partial \left(r\rho u_r\right)}{\partial r} + \frac{1}{r} \frac{\partial \left(\rho u_\theta\right)}{\partial \theta} = 0,\tag{1}$$

$$\begin{split} \frac{\partial \left(\rho u_{z}\right)}{\partial t} + \frac{\partial \left(\rho u_{z} u_{z}\right)}{\partial z} + \frac{1}{r} \frac{\partial \left(r \rho u_{r} u_{z}\right)}{\partial r} + \frac{1}{r} \frac{\partial \left(\rho u_{\theta} u_{z}\right)}{\partial \theta} \\ = -\frac{\partial p}{\partial z} + \frac{\rho}{F r_{0}^{2}} + \frac{1}{R e_{0}} \left(\frac{\partial \tau_{zz}}{\partial z} + \frac{1}{r} \frac{\partial \left(r \tau_{rz}\right)}{\partial r} + \frac{1}{r} \frac{\partial \tau_{\theta z}}{\partial \theta}\right), \end{split} \tag{2}$$

$$\frac{\partial \left(\rho u_r\right)}{\partial t} + \frac{\partial \left(\rho u_z u_r\right)}{\partial z} + \frac{1}{r} \frac{\partial \left(r \rho u_r u_r\right)}{\partial r} + \frac{1}{r} \frac{\partial \left(\rho u_\theta u_r\right)}{\partial \theta} + \frac{\rho u_\theta u_\theta}{r}$$

$$= -\frac{\partial p}{\partial r} + \frac{1}{Re_0} \left(\frac{\partial \tau_{rz}}{\partial z} + \frac{1}{r} \frac{\partial (r \tau_{rr})}{\partial r} + \frac{1}{r} \frac{\partial \tau_{r\theta}}{\partial \theta} - \frac{\tau_{\theta\theta}}{r}\right), \tag{3}$$

$$\frac{\partial \left(\rho u_{\theta}\right)}{\partial t} + \frac{\partial \left(\rho u_{z} u_{\theta}\right)}{\partial z} + \frac{1}{r} \frac{\partial \left(r \rho u_{r} u_{\theta}\right)}{\partial r} + \frac{1}{r} \frac{\partial \left(\rho u_{\theta} u_{\theta}\right)}{\partial \theta} + \frac{\rho u_{r} u_{\theta}}{r}$$

$$= -\frac{1}{r} \frac{\partial p}{\partial \theta} + \frac{1}{Re_{0}} \left(\frac{\tau_{\theta z}}{\partial z} + \frac{1}{r^{2}} \frac{\partial \left(r^{2} \tau_{r\theta}\right)}{\partial r} + \frac{1}{r} \frac{\partial \tau_{\theta \theta}}{\partial \theta}\right), \tag{4}$$

$$\begin{split} &\frac{\partial \left(\rho h\right)}{\partial t} + \frac{\partial \left(\rho u_{z} h\right)}{\partial z} + \frac{\partial \left(\rho u_{r} h\right)}{\partial r} + \frac{1}{r} \frac{\partial \left(\rho u_{\theta} h\right)}{\partial \theta} \\ &= \frac{1}{Re_{0} Pr_{0}} \left(\frac{\partial}{\partial z} \left(\lambda \frac{\partial T}{\partial z}\right) + \frac{1}{r} \frac{\partial}{\partial r} \left(r \lambda \frac{\partial T}{\partial r}\right) + \frac{1}{r} \frac{\partial}{\partial \theta} \left(\lambda \frac{\partial T}{\partial \theta}\right)\right), \end{split} \tag{5}$$

in which $\Psi=(\partial u_z/\partial z)+(1/r)(\partial r u_r/\partial r)+(1/r)(\partial u_\theta/\partial \theta)$ and the viscous stress tensor is written as:

$$\tau_{zz} = \mu \left(2 \frac{\partial u_z}{\partial z} - \frac{2}{3} \Psi \right), \quad \tau_{zr} = \mu \left(\frac{\partial u_z}{\partial r} + \frac{\partial u_r}{\partial z} \right),$$

$$\tau_{z\theta} = \mu \left(\frac{1}{r} \frac{\partial u_z}{\partial \theta} + \frac{\partial u_{\theta}}{\partial z} \right), \quad \tau_{rr} = \mu \left(2 \frac{\partial u_r}{\partial r} - \frac{2}{3} \Psi \right),$$

$$\tau_{r\theta} = \mu \left(\frac{1}{r} \frac{\partial u_r}{\partial \theta} + r \frac{\partial}{\partial r} \left(\frac{u_{\theta}}{r} \right) \right), \quad \tau_{\theta\theta} = \mu \left(2 \left(\frac{1}{r} \frac{\partial u_{\theta}}{\partial \theta} + \frac{u_r}{r} \right) - \frac{2}{3} \Psi \right).$$
(6)

Here z, r and θ are the streamwise, radial and azimuthal coordinates, and in addition, the wall-normal distance, y (= 1 - r), is also

used sometimes. In the above equations, velocities, temperature and thermophysical properties are normalised using their inlet values:

$$u_i = \frac{u_i^*}{u_0^*}, \quad T = \frac{T^*}{T_0^*}, \quad \rho = \frac{\rho^*}{\rho_0^*}, \quad \mu = \frac{\mu^*}{\mu_0^*}, \quad \lambda = \frac{\lambda^*}{\lambda_0^*},$$
 (7)

and lengths are normalised by the radius, the pressure is normalised by $\rho_0^* u_0^* u_0^*$, the enthalpy is shifted by a reference enthalpy h_{ref}^* then normalised:

$$z = \frac{z^*}{R^*}, \quad r = \frac{r^*}{R^*}, \quad r\theta = \frac{r^*\theta^*}{R^*}, \quad p = \frac{p^*}{\rho_0^* u_0^* u_0^*}, \quad h = \frac{h^* - h_{ref}^*}{c_{\pi 0}^* T_0^*}$$
(8)

The enthalpy at $T_0^* + 350$ K is chosen here as h_{ref}^* , so that the fitting curve of the $\rho h - h$ relation can be monotonous, to ensure the numerical stability within the solver when handling drastic variations in enthalpy as well as properties.

CHAPSim is a finite difference solver based on a structured mesh. The second order central difference scheme and third order Runge–Kutta scheme are used for spatial and time discretisations. At each time step, the pressure and velocity fields are corrected by solving the Poisson equation to satisfy both the momentum and continuity equations.

Under the low-Mach number approximation, the influence of the variations of hydrodynamic pressure on the thermophysical properties are negligible, therefore the thermophysical properties are temperature-dependent only. At each time step, when the temperature is solved, the properties are then updated using a property look-up table extracted from the NIST database [38].

In the present study, both the Reynolds-average and the Favre-average are used. For the Reynolds-average, the averaged value is denoted by an over-bar $(\overline{\phi})$ and the fluctuating component is denoted by a single prime (ϕ') . For the Favre-average (density-weighted average), the averaged value is denoted by a over-tilde $(\widetilde{\phi} = \overline{\rho}\phi/\overline{\rho})$, and the fluctuating component is denoted by a double prime (ϕ'') . The average is performed circumferentially as well as over a period of time after the flow has reached a stationary state.

2.2. Implementation of conjugate heat transfer

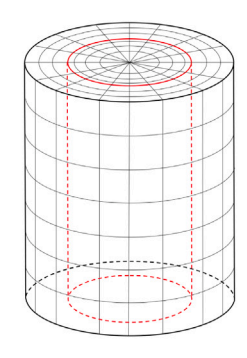
To simulate the thermal conduction within the solid pipe and couple it with the fluid, additional layers of structural mesh is added beyond the boundary of the fluid mesh. In Fig. 1(a), a simplified illustration of the structured mesh in cylindrical coordinate is presented, with the fluid–solid interface highlighted in red. Conformal meshing is used at the fluid–solid interface, and hence, the two domains have the same grid numbers at both streamwise and circumferential directions. The fluid domain has a non-uniform radial mesh distribution while the solid domain has a uniform distribution. The governing equation for the solid is:

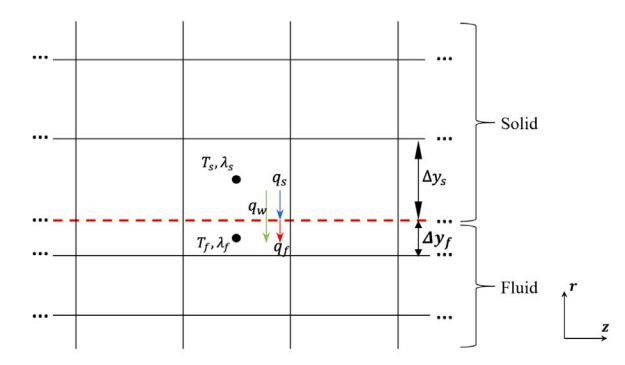
$$\rho_{s}c_{p,s}\frac{\partial T}{\partial t} = \frac{1}{Re_{0}Pr_{0}}\left(\frac{\partial}{\partial z}\left(\lambda_{s}\frac{\partial T}{\partial z}\right) + \frac{1}{r}\frac{\partial}{\partial r}\left(r\lambda_{s}\frac{\partial T}{\partial r}\right) + \frac{1}{r}\frac{\partial}{\partial \theta}\left(\lambda_{s}\frac{\partial T}{\partial \theta}\right) + q_{s}\right),\tag{2}$$

in which subscript s denotes the solid pipe and q_s is the volumetric heating source in the solid:

$$q_s = q_s^* R^{*2} / (\lambda_0^* T_0^*). \tag{10}$$

For the simulation without CHT, only the fluid domain is solved with Neumann boundary condition (wall heat flux) applied at the boundary. While for the CHT simulation, an equivalent volumetric heating source is uniformly applied to the solid body. At each time step, the local heat flux across the fluid–solid interface is evaluated explicitly using information at both the solid and fluid domain from the last time step. This heat flux is then imposed as the thermal boundary condition for both the fluid and solid domains, to ensure energy conservation.





(a) Structural mesh in cylindrical coordinate

(b) Heat flux at the fluid-solid interface

Fig. 1. Example structured mesh for fluid and solid domains, with fluid mesh size of $7 \times 4 \times 16$ (streamwise \times radial \times spanwise), and solid mesh size of $7 \times 4 \times 16$ (a), and a zoom-in z-r plane close to the fluid-solid interface.

Fig. 1b shows an enlarged view of the mesh around the fluid–solid interface (red-dash line), the lower and upper part denote the fluid and solid mesh. Temperatures and thermal conductivities are defined at the cell centre. Subscripts "s", "f" and "w" represent values in the solid, fluid and at the interface, respectively. q_s (blue) is the heat flux leaving the solid, q_f (red) is the heat flux enters the fluid. The heat fluxes from the fluid and the solid are calculated as:

$$q_s = \lambda_s \frac{T_s - T_w}{\Delta y_s / 2}, \qquad q_f = \lambda_f \frac{T_w - T_f}{\Delta y_f / 2}. \tag{11}$$

To ensure energy conservation and temperature continuity, we let $q_s=q_f$, and $T_{ws}=T_{wf}$, which leads to:

$$\lambda_s \frac{T_s - T_w}{\Delta y_s / 2} = \lambda_f \frac{T_w - T_f}{\Delta y_f / 2}.$$
 (12)

Then q_w can be solved from rearranging Eq. (12):

$$q_w = \frac{2\lambda_s \lambda_f (T_s - T_f)}{\lambda_f \Delta y_s + \lambda_s \Delta y_f}$$
 (13)

In the above calculations, a local heat flux q_w is evaluated explicitly using the information from the solid and fluid domain at the current time step. It is then applied to the interface as Neumann boundary condition for the solid and fluid domain at next time step.

2.3. Case settings

One of the experiments in [33] with a strong heating and a Reynolds number of 3600 (based on pipe diameter) is selected as a reference of interest in the present study. This is an upward pipe flow of carbon dioxide at 7.6 MPa with an inlet temperature of 295.15 K, a wall heat flux of 63 kW/m² and a pipe (inner) diameter of 0.953 mm and wall thickness of 0.53 mm. In the present study, the experiment is reproduced in DNS with and without CHT. The configurations of the two models are shown in Fig. 2.

Both cases simulate a pipe of a length of 50D, corresponding to the heat transfer deterioration stage observed in the experiment. In Case CHT, the solid pipe wall is made of stainless steel (SS 304) and it has an inner & outer diameter of 0.953 mm and 2.01 mm according to the experiment specifications [33]. The thermal activity ratio K [17,39] for Case CHT is 0.061, suggesting a significant damping effect according to the literature. A volumetric heat source of 204.85 kW/m³ is uniformly applied to the solid, which is equivalent to the wall heat flux of 63 kW/m² applied at the fluid boundary in Case NoCHT. Adiabatic boundary condition is applied at the solid outer surface in Case CHT.

2.4. Mesh

A structured, cylindrical mesh is used in the CHAPSim solver. The mesh for the fluid in the two cases is the same: the grid numbers at the streamwise, radial and spanwise directions are $1280 \times 64 \times 128$, with their resolutions of $\Delta z^{+0} = 9.59$, $\Delta y^{+0} = 0.12 \sim 5.04$ and $R\Delta \theta^{+0} = 6.03$ based wall units at $Re_0 = 3600$. The mesh is similar to those in [10] ($\Delta z^+ = 14.55$, $\Delta y^+ = 0.18 \sim 5.34$ and $R\Delta \theta^+ = 9.14$, $Re_0 = 5400$) and [13] ($\Delta z^+ = 6.25$, $\Delta y^+ = 0.55 \sim 4.31$ and $R\Delta \theta^+ = 3.93$, $Re_0 = 5400$).

Validations and grid convergence study of solver CHAPSim against flows similar to the condition of interest here were conducted and presented in [40]. An isothermal pipe flow at $Re_{\tau} = 180$ from [41] was reproduced and good agreements were shown in the mean velocity profile and profiles of root-mean-square of fluctuating velocities. For the flow condition of interest, two cases of upward pipe flow of supercritical carbon dioxide at $Re_0 = 5400$ in [10,13] were reproduced using CHAPSim. Good agreements in wall temperatures, profiles of mean velocity and turbulent shear stress were shown between the results from the three solvers. Furthermore, a grid convergence study was carried out based on an upward pipe flow of supercritical carbon dioxide at $Re_0 = 5400$. The simulation was run at two mesh resolutions (1024×64×128 and 2048×128×128), with the grid numbers at streamwise and radial directions doubled in the case with a finer mesh. The profiles of mean velocity and turbulent shear stress in the two cases agree well with each other [40], indicating the result is independent of mesh resolution.

3. Results and discussions

3.1. Heat transfer

The heat transfer coefficients (HTC) and wall temperatures for both Case NoCHT and Case CHT, as well as those obtained from the experiment conducted by Luo [33], are presented in Fig. 3a and 3b. The HTC obtained via the Gnielinski correlation [42,43] is also included as a reference representing the HTC in fully-developed, forced convection flows with the same local condition. The Gnielinski correlation is written as:

$$HTC_{fc} = Nu_{fc}\lambda_b^*/D^*, \ \ Nu_{fc} = \frac{(f_D/8)(Re_D - 1000)Pr}{1 + 12.7(f_D/8)^{1/2}(Pr^{2/3} - 1)}, \eqno(14)$$

in which f_D is the Darcy friction factor: $f_D = (0.79ln(Re_D) - 1.64)^{-2}$.

Overall, the general trend observed in the experiment has been reasonably well captured in both simulations: HTC reduces rapidly then levels off at z/D>30, while the wall temperature progressively increases in the streamwise direction. At most locations except the initial part, HTC are lower than their corresponding forced convection values (HTC_{fc}), indicating the occurrence of heat transfer deteriorations (HTD) in both cases. When HTC in both cases reduce to a low-level at z/D>30, they agree well with the measurement. A detailed inspection shows that Case CHT yields a slightly better prediction of HTC and wall temperature during the HTD process in comparison with NoCHT. In NoCHT, the HTC around z/D=10 to 20 is slightly over-predicted and

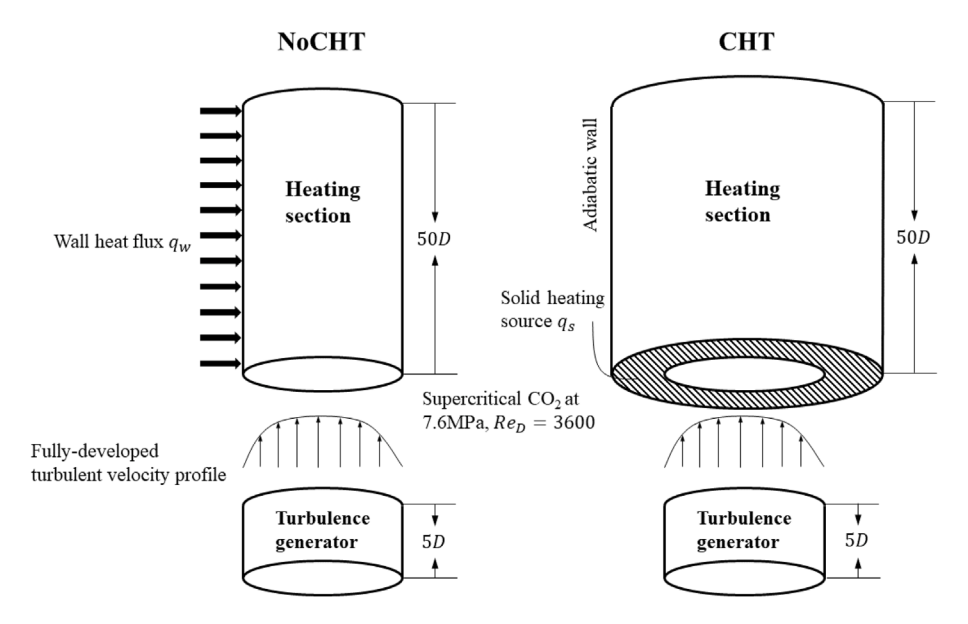


Fig. 2. Schematic diagram of cases NoCHT (left) & CHT (right).

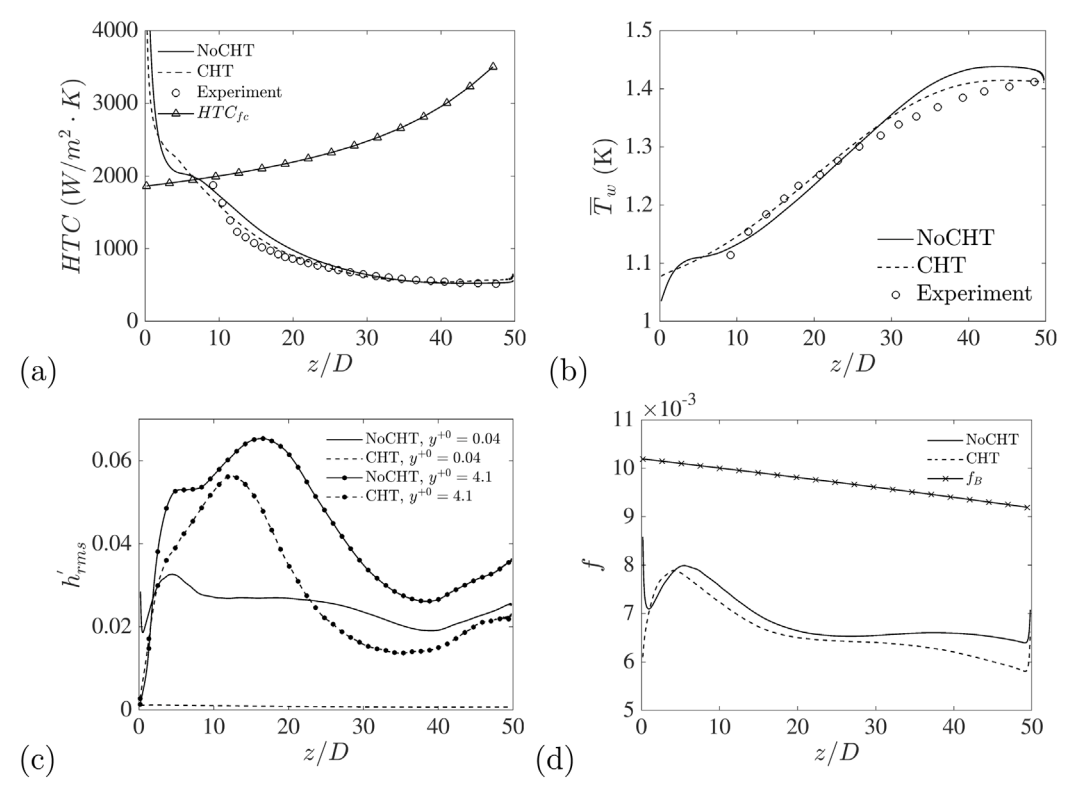


Fig. 3. Heat transfer coefficients (a), wall temperatures (b), root-mean-square of enthalpy fluctuations close to the wall (c) and Fanning friction factors (d) in Cases NoCHT and CHT

 T_w after $z/D \approx 30$ is over-predicted, and these discrepancies are to some extent mitigated when conjugate heat transfer is introduced.

The root-mean-square (rms) of enthalpy fluctuations $(h'_{rms} = \sqrt{\overline{hh} - \overline{h} \, \overline{h}})$ near the wall (at $y^{+0} = 0.04$ and 4.1) in both cases are shown in Figs. 3c. When CHT is introduced, the enthalpy fluctuations are notably dampened by a factor of 30 on average at $y^{+0} = 0.04$ (Fig. 3c). However, this effect diminishes rapidly away from the wall: at $y^{+0} = 4.1$, the difference between the rms fluctuations in NoCHT and CHT is reduced to 1.6 times. Potentially, the dampening of enthalpy fluctuations leads to a corresponding reduction in the fluctuating

level of density, which in turn affects the buoyancy production term for turbulent kinetic energy. According to the literature on similar flow problems [10,15], buoyancy production is non-negligible at the laminarising stage and becomes pre-dominant at the recovery stage. This suggests that the dampened enthalpy fluctuations might eventually impact the turbulence via the buoyancy production and this will be further examined later.

In Fig. 3d, the Fanning friction factor $f = 2\tau_w^*/\rho_b^* \mu_b^{*2}$ in both cases are shown, along with those obtained using the Blasius correlation $f_B = 0.0791/Re^{0.25}$ [44], representing the reference values for forced-convection pipe flows at the corresponding local condition. Initially, f

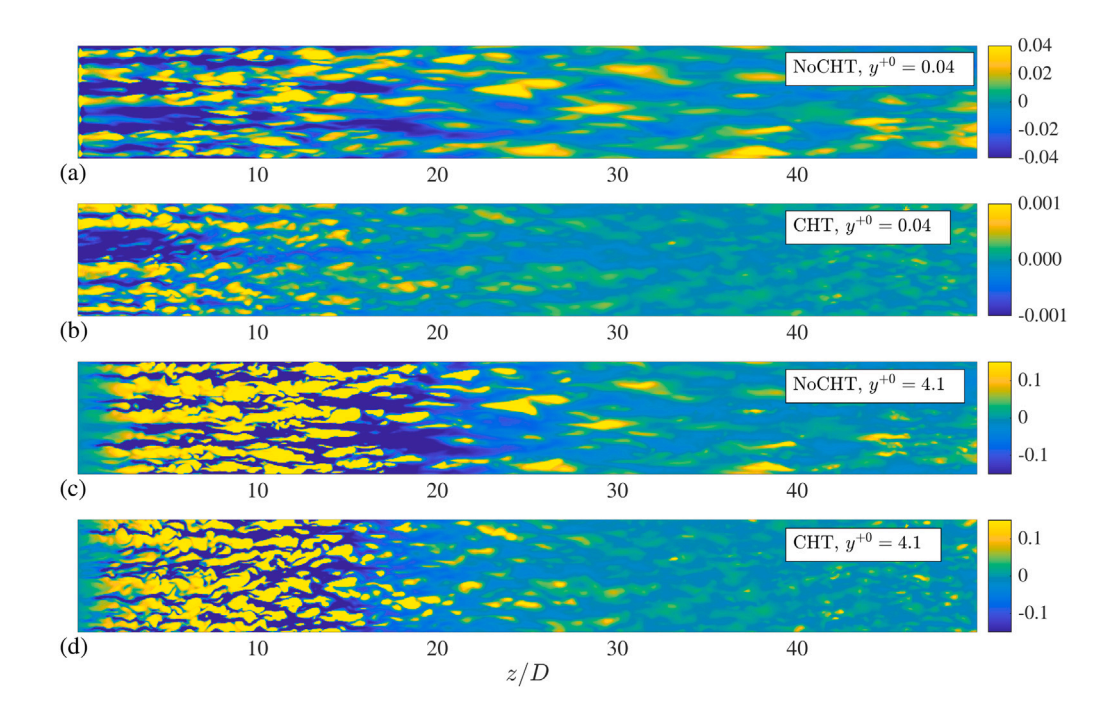


Fig. 4. Instantaneous density fluctuations in NoCHT and CHT at near-wall planes at $y^{+0} = 0.04$ (a and b) and 4.1 (c and d).

exhibits significant differences between the two cases, attributed to the more rapidly established thermal boundary layer and correspondingly a significantly lower near-wall viscosity in Case CHT. At further downstream, f in both cases show a similar trend, with an increase shortly followed by a gradual decrease due to the development of the mean velocity profile. The peak in f appears at a lower height in Case CHT, indicating that the flow development in CHT is slightly ahead. f in both cases are lower than their forced-convection values (f_B), suggesting they both exhibit a weakening turbulence mixing since the beginning. Compared to the HTCs, the impact of CHT on f is relatively small and confined to the region close to the inlet.

The damping effect is more clearly illustrated in Fig. 4, which shows the instantaneous density fluctuations ($\rho' = \rho - \overline{\rho}$) at two near-wall planes ($y^{+0} = 0.04$ and 4.1) in Case NoCHT and Case CHT. They are very different near the wall at $y^{+0} = 0.04$ but rather similar further away at $y^{+0} = 4.1$. At $y^{+0} = 0.04$ in Case NoCHT, frequent and intensive spatial variations in ρ' are observed, displayed in the form of coherent structures. The amplitudes reduce at a later location when the flow is laminarising, with coherent structures broken. In Case CHT, ρ' exhibits a much weaker magnitude (Fig. 4b), hence the colour scale has been reduced by 40 times so as to clearly visualise the distribution. Similar to those in Case NoCHT, coherent structures appear after the inlet and they are broken-down rapidly when the flow is being 'laminarised'. Whilst ρ' at $y^{+0} = 4.1$ (further away but still very close to the wall) appears rather similar between Case NoCHT and Case CHT (Fig. 4c and 4d). In both cases, the spatial variations are frequent and intensive at initial locations, and both experience stabilisation when the flow is 'laminarised' at the later stage. This comparison indicates that although considering CHT potentially dampens the fluctuations in enthalpy and thermal properties, this effect is limited to a small region very close to the wall and diminishes rapidly further away, at least for the condition of interest in the present study. It also suggests that the influences on mean-flow and turbulence characteristics might be somewhat limited, which will be further explored in the next section.

The axial distributions of the wall heat flux in both cases are shown in Fig. 5. In Case NoCHT, the wall heat flux is uniformly distributed,

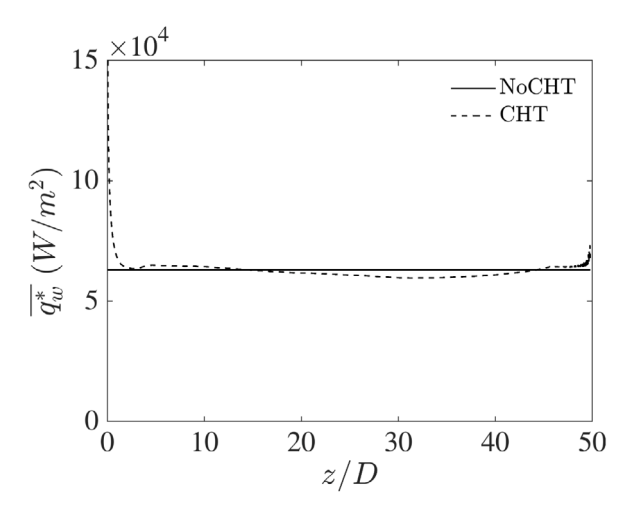


Fig. 5. Axial distributions of wall heat flux in NoCHT and CHT.

whereas in Case CHT it is redistributed, reaching magnitudes of 2 to 3 times of those in NoCHT within z/D < 1.5 close to the inlet. Because of this, the establishment of thermal boundary layer (ThBL) is more rapid in Case CHT, indicating by the mean-temperature profiles (that will be shown later) as well as the rapid reduction in HTC close to the inlet, shown in Fig. 3a. The inclusion of CHT has a major influence on the development of the wall temperature close to the inlet. Without CHT, the wall temperature increases from the inlet temperature rapidly within the first few pipe-diameter distance, followed by gradual changes. With CHT, the streamwise conduction redistributes the wall heating energy towards upstream as shown earlier, which has caused the wall temperature rise significantly, making the streamwise wall temperature change much smoother. We expect this to be more realistic in physical experiment.

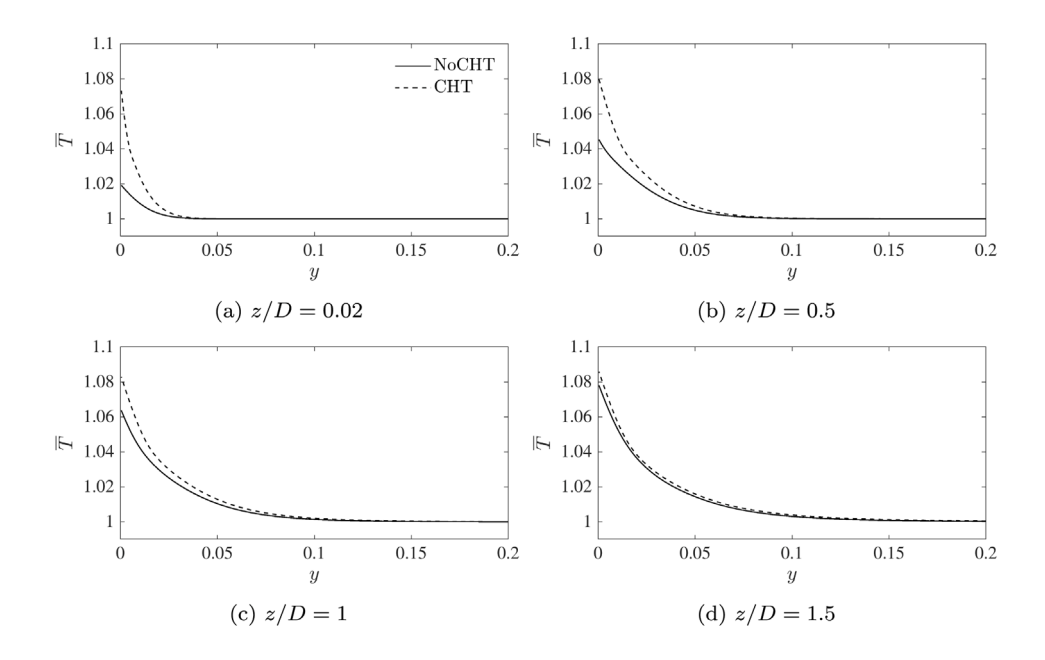


Fig. 6. Mean-temperature profiles close to the wall (y < 0.2) at initial streamwise locations.

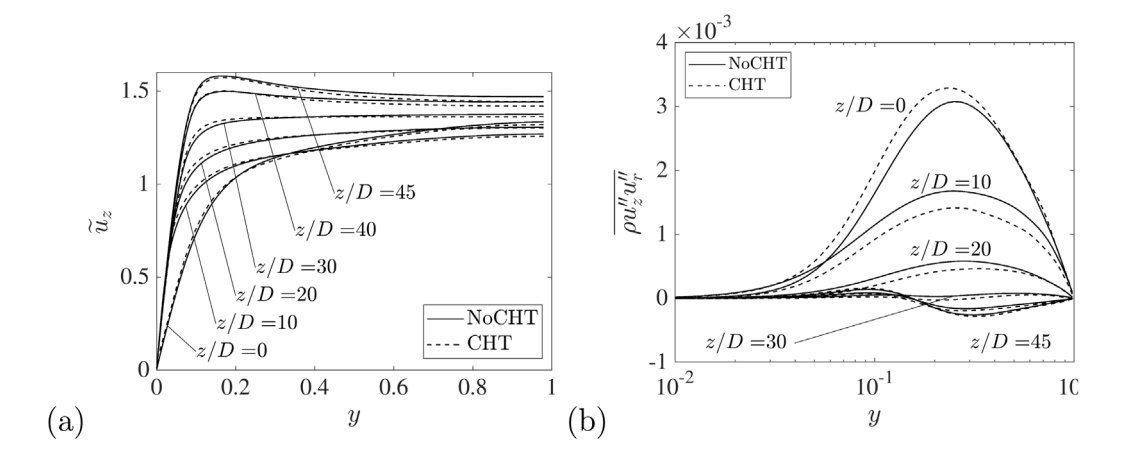


Fig. 7. Favre-averaged velocity (a) and turbulent shear stress (b) in cases NoCHT and CHT.

The mean-temperature profiles near the wall at initial streamwise locations (z/D < 1.5) are shown in Fig. 6, demonstrating the establishment of the ThBL in both cases. They both have an inflow with a uniform temperature (T = 1) at z/D = 0 where heating starts. Within the thermal entrance region (TER) where ThBL is forming, heat transfer is significantly higher than that of a (thermally) fullydeveloped flow, as evidenced by the much higher HTC at entrance locations shown in Fig. 3a. Such enhancement in heat transfer, however behaves differently in the two cases: In Case NoCHT, a uniform heat flux is applied at the wall, resulting in a gradual establishment of the ThBL. Whereas in Case CHT, the wall heat flux is redistributed axially, via thermal conduction in the solid, with a certain amount of heat redistributed upstream, leading to a much higher local wall heat flux in the TER, as shown in Fig. 5. Consequently, the establishment of the ThBL in Case CHT appears more abrupt and rapid, with a significantly higher wall temperature at z/D = 0.02 compared to Case NoCHT. This more rapid establishment of ThBL, as a result of the heat redistribution introduced by CHT, is usually not captured in DNS that a uniform heat

flux applied to the wall. However, at z/D=1.5, the ThBL in both cases are formed the two mean-temperature profiles become very similar, indicating that this impact is largely confined within a short distance at the streamwise direction.

3.2. Mean flow and turbulence

The profiles of the Favre-averaged velocity and turbulent shear stress at several selected locations in Case NoCHT and Case CHT are shown in Fig. 7. The evolutions of \widetilde{u}_z and $\rho u_z'' u_r''$ in the two cases are similar: \widetilde{u}_z is initially flattened then becomes M-shape due to acceleration close to the wall and deceleration in the mainstream. Simultaneously, $\rho u_z'' u_r''$ rapidly decreases as flow undergo laminarisation and becomes negative at further downstream. This trend has been observed in various relevant studies [10,13,15,45] regarding the upward heated flows of supercritical fluids and it is a typical and well-known phenomenon that has been extensively studied. Instead of further exploring the

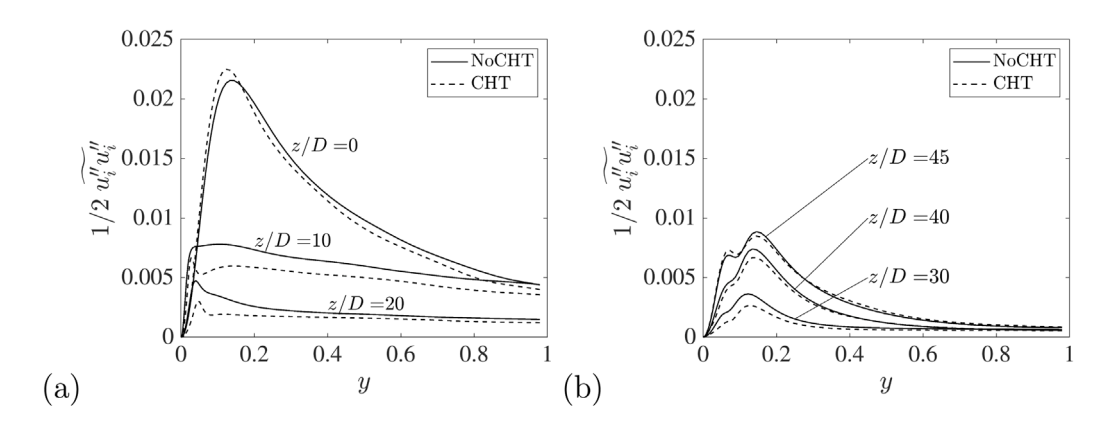


Fig. 8. Turbulent kinetic energy in cases NoCHT and CHT: (a) the profiles for z/D = 0, 10 and 20; (b) the profiles for z/D = 30, 40 and 45.

phenomena, our focus here is on the impact of conjugate heat transfer. In Case CHT, the developments in the mean-velocity and turbulent shear stress are slightly ahead due to an earlier established ThBL, except those at the very initial locations. During the laminarising progress (z/D < 30), $\overline{\rho u_2'' u_r''}$ in Case CHT is lower than the other, indicating the occurrence of a more rapidly progressing laminarising process, which might be responsible for the lower HTC in Case CHT at z/D = 10 to 20 (Fig. 3a). This will be comprehended via the decomposition of the Nusselt number in the later section.

The profiles of turbulent kinetic energy (TKE) are shown in Fig. 8. Again, the variations in Case NoCHT and CHT exhibit a similar trend: TKE decreases rapidly before z/D=30 when the flow is laminarising (hence we define this region as the 'laminarising' region), followed by a recovery. This is consistent with the variation in turbulent shear stress, which reduces to nearly zero everywhere at z/D=30. Notably, TKE develops to a two-peak profile when turbulence is recovered, same as those observed in [46]. The differences in TKE between cases NoCHT and CHT are relatively large at z/D=10, 20 and 30 when the flow is laminarising, compared to those after z/D=30. At z/D=10, 20 and 30, the peak of TKE in Case NoCHT is 1.17, 1.55 and 1.37 times of that in Case CHT, then at z/D=40 and 45, they are very similar.

In the current state-of-art understanding of the 'laminarisation' and recovery in upward heated flows of supercritical fluid, the indirect effect of buoyancy predominantly influences the 'laminarising' stage, while the direct effect contributes significantly to the recovery. The indirect effect is characterised by the altered mean-velocity profile, leading to a reduction in shear production. The direct effect comes from the buoyancy production induced by density fluctuations. To inspect the variations of these effects within cases NoCHT and CHT, profiles of shear production and buoyancy production at various locations of interest (z/D = 0 to 36) are shown in Fig. 9. These terms are in Favre-average form, with shear production represented as P_k $-\overline{\rho u_i'' u_i''}(\partial \widetilde{u_i}/\partial x_i)$ and buoyancy production as $G_k = -\overline{u_i''}(\partial \overline{p}/\partial z)$. From z/D = 0 to 36, both flows transition from a state dominated by the indirect effect to another state dominated by the direct effect: at z/D = 0, G_k is zero everywhere and P_k has a large peak close to the wall, while at z/D = 36, P_k is zero everywhere and G_k peaks near the wall. At z/D = 0, the peak of P_k in Case CHT is slightly higher than that in Case NoCHT, likely linked to the more rapid establishment of thermal boundary layer, though further investigation is needed to reveal the mechanisms. From z/D = 4 to 20, P_{ν} continuously decreases, with Case CHT progressing ahead. Buoyancy production G_k is negative with a significant magnitude, extracting energy from turbulence to the mean flow and accelerating the 'laminarisation' process [10,15]. Here, the peak of G_k in Case CHT is slightly higher than that in Case NoCHT. From z/D = 24, P_k in both cases decreases and maintains at a low level,

while G_k progressively increases. During this process, the magnitudes of P_k and G_k are very similar in both Case NoCHT and Case CHT.

3.3. Decomposition of Nusselt number

To inspect different factors that impact the heat transfer, the Nusselt numbers in the two cases are decomposed using the Fukagata, Iwamoto & Kasagi (FIK) decomposition [47,48]. The full formula of the FIK-decomposition for a vertical pipe flow is written as:

$$Nu_{\text{FIK}} = \underbrace{\frac{8}{\alpha_{b} \left(\overline{h_{w}} - h_{b}\right)} \int_{0}^{1} r \bar{\alpha} \frac{\partial \bar{h}}{\partial r} r dr - \frac{8Re_{b0}Pr_{0}}{\alpha_{b} \left(\overline{h_{w}} - h_{b}\right)} \int_{0}^{1} r \rho h'' u_{r}'' r dr}_{A_{b} \left(\overline{h_{w}} - h_{b}\right)} \int_{0}^{1} \left(R^{2} - r^{2}\right) \left\langle \frac{1}{r} \frac{\partial r \bar{\rho} h \bar{u}_{r}}{\partial r} \right\rangle r dr}_{Nu_{1} \left(\overline{h_{w}} - h_{b}\right)} \int_{0}^{1} \left(R^{2} - r^{2}\right) \left\langle \frac{1}{r} \frac{\partial r \bar{\rho} h \bar{u}_{r}}{\partial r} \right\rangle r dr}_{Nu_{3}}$$

$$- \frac{4Re_{0}Pr_{0}}{\alpha_{b} \left(\overline{h_{w}} - h_{b}\right)} \int_{0}^{1} \left(R^{2} - r^{2}\right) \left\langle \frac{\partial \bar{\rho} h \bar{u}_{z}}{\partial z} \right\rangle r dr}_{Nu_{4}}$$

$$- \frac{4Re_{0}Pr_{0}}{\alpha_{b} \left(\overline{h_{w}} - h_{b}\right)} \int_{0}^{1} \left(R^{2} - r^{2}\right) \left\langle \frac{\partial \bar{\rho} h'' u_{z}''}{\partial z} \right\rangle r dr}_{Nu_{5}}$$

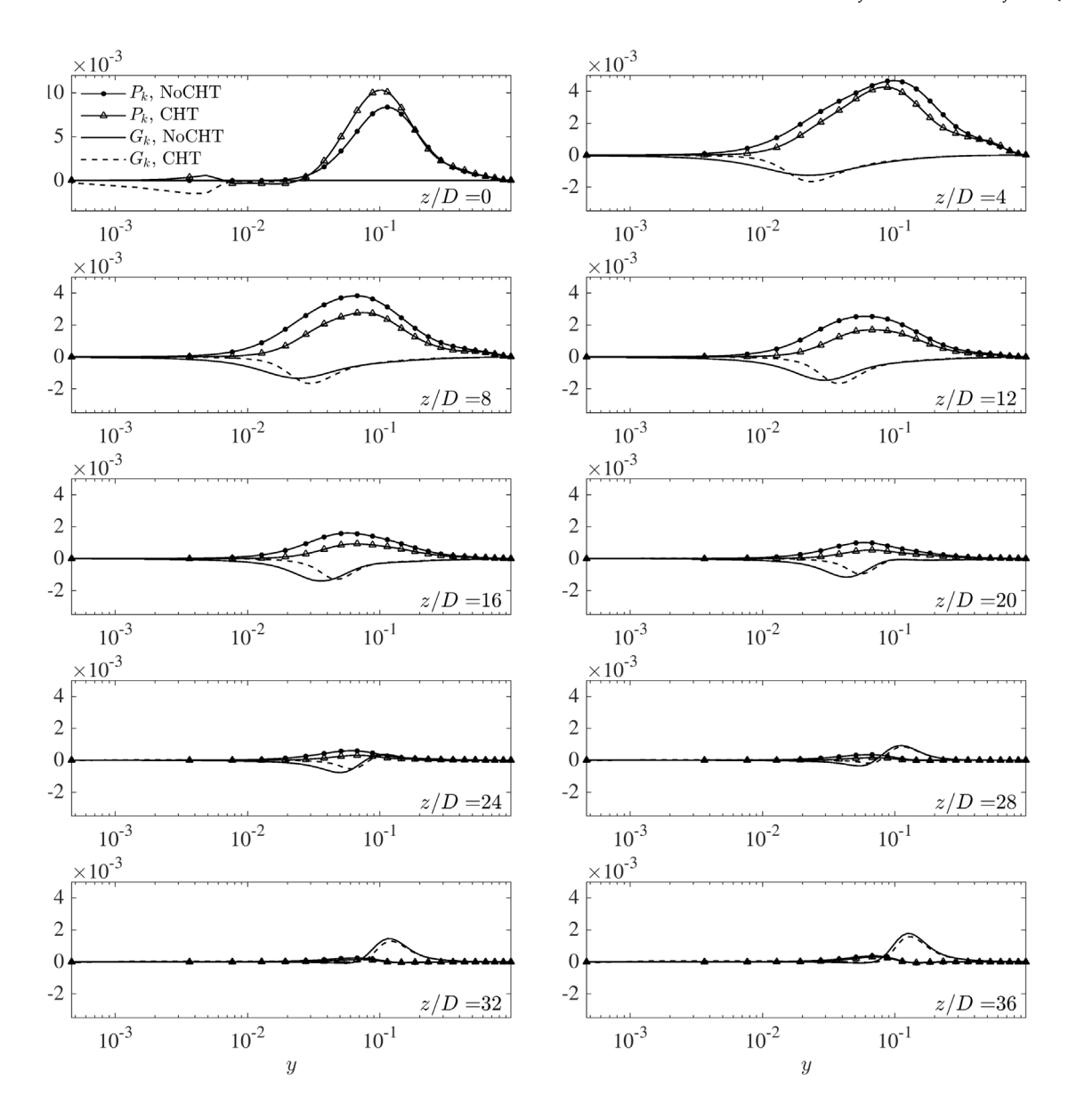
$$+ \frac{4}{\alpha_{b} \left(\overline{h_{w}} - h_{b}\right)} \int_{0}^{1} \left(R^{2} - r^{2}\right) \left\langle \frac{1}{r} \frac{\partial r}{\partial r} \alpha' \frac{\partial h'}{\partial r} \right\rangle r dr}_{Nu_{6}}$$

$$+ \frac{4}{\alpha_{b} \left(\overline{h_{w}} - h_{b}\right)} \int_{0}^{1} \left(R^{2} - r^{2}\right) \left\langle \frac{\partial}{\partial z} \left(\bar{\alpha} \frac{\overline{\partial h}}{\partial z}\right) \right\rangle r dr}_{Nu_{7}}$$

$$+ \frac{4}{\alpha_{b} \left(\overline{h_{w}} - h_{b}\right)} \int_{0}^{1} \left(R^{2} - r^{2}\right) \left\langle \frac{\partial}{\partial z} \left(\bar{\alpha}' \frac{\overline{\partial h'}}{\partial z}\right) \right\rangle r dr}_{Nu_{7}}$$

in which " $\langle \ \rangle$ " represents the following operator:

$$\langle \phi(r,z) \rangle = \phi(r,z) - \frac{2}{R^2} \int_0^R \phi(r,z) r dr. \tag{16}$$



 $\textbf{Fig. 9.} \ \ \textbf{Shear} \ \ \textbf{production} \ \ \textbf{and} \ \ \textbf{buoyancy} \ \ \textbf{production} \ \ \textbf{of} \ \ \textbf{TKE} \ \ \textbf{in} \ \ \textbf{cases} \ \ \textbf{NoCHT} \ \ \textbf{and} \ \ \textbf{CHT}.$

In Eq. (15), Nu_1 represents the laminar contribution, Nu_2 represents the contribution based on the radial turbulent heat flux $-\rho u_I'' h^{II}$, Nu_3 and Nu_4 represent the contributions from the radial and streamwise advections, Nu_5 represents the contribution from the streamwise turbulent heat flux $-\rho h'' u_I''$, Nu_6 , Nu_8 represent the contributions from the fluctuations of the radial and streamwise heat flux, Nu_7 represents the contribution from the thermal conduction at streamwise direction. Nu_3 to Nu_8 are referred to as the inhomogeneous contributors. The influences of Nu_5 to Nu_8 are found to be negligible [19,40].

The Nusselt numbers in both Case NoCHT and Case CHT, along with their Nu_{FIK} , are shown in Fig. 10a. Here only Nu_1 to Nu_4 are considered for Nu_{FIK} and the rest terms are omitted. The qualitative agreement between Nu and Nu_{FIK} supports the reliability of formula (15) and indicates that Nu_5 to Nu_8 are negligible to some extent. To simplify the discussion, the laminar contribution Nu_1 , turbulent contribution Nu_2 and inhomogeneous contribution $Nu_3 + Nu_4$ are denoted as Nu_l , Nu_t and Nu_{lh} , respectively. The comparisons of these terms between Case NoCHT and Case CHT are shown in Fig. 10b to 10d.

The laminar contribution represents the impact of the profile of mean-enthalpy on heat transfer. Differences are observed between Nu_1 in the two cases especially at initial location (z/D < 10). In Case CHT, Nu_l starts at a much lower level, while in Case NoCHT, it experiences a drastic decrease. This is attributed to a more rapid establishment of thermal boundary layer in Case CHT and it is corresponding to the difference in HTC close to the inlet. At later locations, Nu_l in both cases progressively decreases with similar magnitudes. The turbulent contribution Nu_t , representing the enhanced heat transfer due to turbulent mixing, exhibits similar trends in both cases: an initial increase followed by a reduction after the peak. However, compared to Case NoCHT, the peak of Nu, in Case CHT is lower by 12.3% and it appears slightly earlier, resulting in a much lower Nu_t from z/D = 10 to 20. Such deficiency, is responsible for the lower HTC during the laminarising process (z/D = 10 to 20) shown in Fig. 3a. The inhomogeneous contribution Nu_{ih} , reflecting the impact from the advection terms at both streamwise and radial directions, are rather similar between the two cases, except that Case CHT shows a slightly earlier reduction at the beginning. Similar to the differences in Nu_l ,

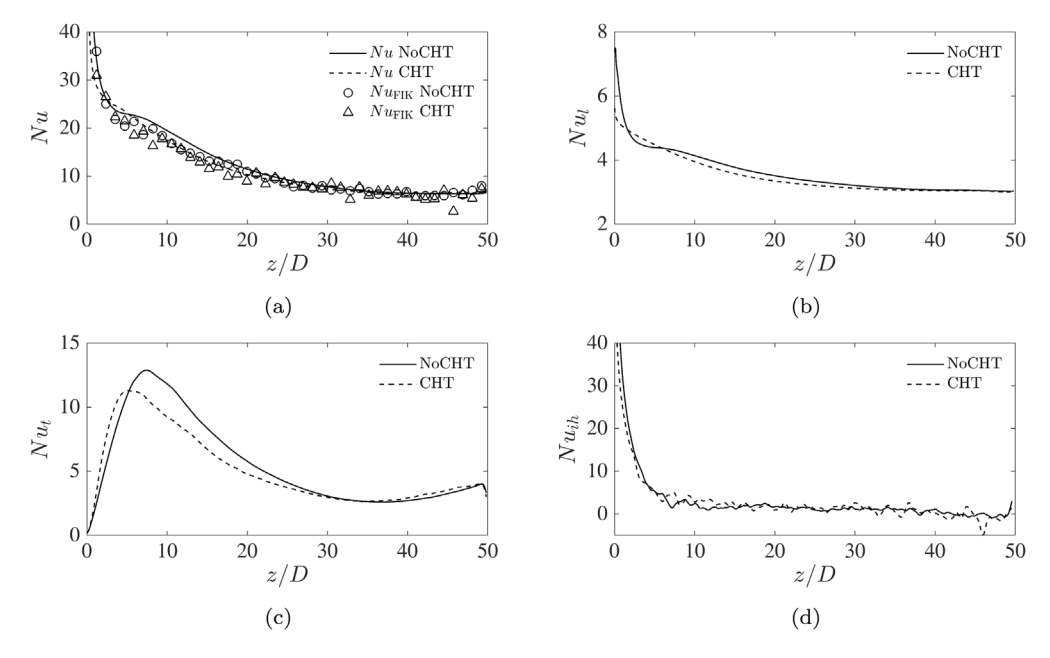


Fig. 10. FIK decomposition for the Nusselt numbers in NoCHT & CHT: $Nu\&Nu_{FIK}$ (a), laminar contributions (b), turbulent contributions (c) and inhomogeneous contributions (d) in the two cases

this is as well attributed to the earlier establishment of the thermal boundary layer. In summary, the first factor brought by conjugate heat transfer, which is the redistribution of wall heating, has a more pronounced impact on the Nusselt than the second one, the near-wall damping.

4. Conclusions

Direct numerical simulations (DNS) of upward heated pipe flows of supercritical CO_2 at $Re_0=3600$ (based on pipe diameter) were conducted with and without considering conjugate heat transfer (CHT). The condition of interest is chosen from an experimental study by Luo [33] and comparisons were performed between the numerical and experimental results. The present study aims at (i) revealing the impact of CHT in DNS for this specific flow problem and (ii) offer information for addressing potential discrepancies caused by the thermal boundary condition in numerical simulations. The impacts of CHT on heat transfer and turbulence were investigated and key findings and conclusions include:

- For the specific condition of interest in the present study, considering CHT in DNS, in comparison with the case without considering, results in slightly improved predictions in heat transfer coefficients and wall temperatures based on the experimental measurements obtained in [33]. Notably, the most significant differences in heat transfer occur at the initial region close to the inlet due to the redistributed wall heat flux and a more rapid establishment of the thermal boundary layer (ThBL).
- The damping effect introduces notable differences in the fluctuation levels in enthalpy as well as thermophysical properties.
 Fluctuations in enthalpy and density are dampened by the factor of 30 and 40 on averaged. However, such impact is confined within a small region very close to the wall and diminishes rapidly away from the wall.
- When CHT is considered, the 'laminarisation' progresses more rapidly due to a more rapidly established ThBL and it has a lower turbulent kinetic energy (TKE) compared to the case without CHT. This is attributed to the discrepancies in shear production rather than buoyancy production in the TKE budget terms. Although the near-wall density fluctuations are dampening by a

factor of 40 when CHT is introduced, it has a minor impact on the buoyancy production term.

• With CHT introduced, both the laminar (Nu_l) and turbulent contributions (Nu_l) to the Nusselt number are altered: Nu_l starts at a lower level near the inlet due to a more rapidly established ThBL, while the peak of Nu_l is lowered by 12.3%. These changes respectively correspond to the discrepancies of HTC close to the inlet and at z/D=10 to 20.

In this study, some differences in turbulence and heat transfer introduced by considering CHT were identified, while certain mechanisms or factors remain unexplored, providing potential directions for future studies: (i) The initial increase in shear production observed in Case CHT is likely linked to the more rapid establishment of the thermal boundary layer. Further investigations are needed to comprehend this process; (ii) A noteworthy limitation in Case CHT is that the solid domain begins at the beginning of the heating section, while the solid pipe featured in experiments normally extends upstream to cover the flow-development section. Addressing this in the simulation could significantly influence the redistribution of wall heating, potentially leading to further improvement in the predictions against experiment measurements.

CRediT authorship contribution statement

Jundi He: Writing – review & editing, Writing – original draft, Visualization, Validation, Methodology, Investigation, Formal analysis. Wei Wang: Writing – review & editing, Validation, Software, Methodology, Investigation. Bing Xu: Writing – review & editing, Formal analysis. Shuisheng He: Writing – review & editing, Supervision, Project administration, Methodology, Investigation, Funding acquisition, Formal analysis, Conceptualization.

Declaration of competing interest

The authors declare that they have no known competing financial interests or personal relationships that could have appeared to influence the work reported in this paper.

Data availability

Data will be made available on request.

Acknowledgement

This work used the ShARC and Stanage high-performance computing service at the University of Sheffield. New developments on CHAPSim have been carried out under the Collaborative Computational Project for Nuclear Thermal Hydraulics (CCP-NTH, EP/T026685/1). The authors gratefully acknowledge the help provided by Dr Wei Wang on solver CHAPSim.

References

- [1] P. Bourke, D. Pulling, L. Gill, W. Denton, Forced convective heat transfer to turbulent CO2 in the supercritical region, Int. J. Heat Mass Transfer 13 (8) (1970) 1339–1348.
- [2] K. Yamagata, K. Nishikawa, S. Hasegawa, T. Fujii, S. Yoshida, Forced convective heat transfer to supercritical water flowing in tubes, Int. J. Heat Mass Transfer 15 (12) (1972) 2575–2593.
- [3] B. Shiralkar, P. Griffith, The effect if swirl, inlet conditions, flow direction, and tube diameter on the heat transfer to fluids at supercritical pressure, J. Heat Transfer 92 (1970) 490–497.
- [4] J. Jackson, M. Cotton, B. Axcell, Studies of mixed convection in vertical tubes, Int. J. Heat Fluid Flow 10 (1) (1989) 2–15.
- [5] V. Kurganov, A. Kaptil'Ny, Velocity and enthalpy fields and eddy diffusivities in a heated supercritical fluid flow, Exp. Thermal Fluid Sci. 5 (4) (1992) 465–478.
- [6] P.X. Jiang, Y.J. Xu, J. Lv, R.F. Shi, S. He, J. Jackson, Experimental investigation of convection heat transfer of CO2 at super-critical pressures in vertical mini-tubes and in porous media, Appl. Therm. Eng. 24 (8–9) (2004) 1255–1270.
- [7] J. Jackson, Fluid flow and convective heat transfer to fluids at supercritical pressure, Nucl. Eng. Des. 264 (2013) 24–40.
- [8] Z.H. Li, P.X. Jiang, C.R. Zhao, Y. Zhang, Experimental investigation of convection heat transfer of CO2 at supercritical pressures in a vertical circular tube, Exp. Therm. Fluid Sci. 34 (8) (2010) 1162–1171.
- [9] J. Yan, Y. Zhu, R. Zhao, S. Yan, P. Jiang, Experimental investigation of the flow and heat transfer instabilities in n-decane at supercritical pressures in a vertical tube, Int. J. Heat Mass Transfer 120 (2018) 987–996.
- [10] J.H. Bae, J.Y. Yoo, H. Choi, Direct numerical simulation of turbulent supercritical flows with heat transfer, Physics Fluids 17 (10) (2005) 105104.
- [11] J.H. Bae, J.Y. Yoo, D.M. McEligot, Direct numerical simulation of heated CO 2 flows at supercritical pressure in a vertical annulus at Re=8900, Phys. Fluids 20 (5) (2008) 055108.
- [12] J.Y. Yoo, The turbulent flows of supercritical fluids with heat transfer, Annu. Rev. Fluid Mech. 45 (2013) 495–525.
- [13] H. Nemati, A. Patel, B.J. Boersma, R. Pecnik, Mean statistics of a heated turbulent pipe flow at supercritical pressure, Int. J. Heat Mass Transfer 83 (2015) 741–752.
- [14] J.W. Peeters, R. Pecnik, M. Rohde, T. Van Der Hagen, B.J. Boersma, Turbulence attenuation in simultaneously heated and cooled annular flows at supercritical pressure, J. Fluid Mech. 799 (2016) 505–540.
- [15] J. He, R. Tian, P. Jiang, S. He, Turbulence in a heated pipe at supercritical pressure, J. Fluid Mech. 920 (2021).
- [16] A. Pucciarelli, W. Ambrosini, On the effect of conjugate heat transfer on turbulence in supercritical fluids: Results from a LES application, Ann. Nucl. Energy 111 (2018) 340–346.
- [17] I. Tiselj, E. Pogrebnyak, C. Li, A. Mosyak, G. Hetsroni, Effect of wall boundary condition on scalar transfer in a fully developed turbulent flume, Phys. Fluids 13 (4) (2001) 1028–1039.
- [18] B.S. Petukhov, A. Polyakov, B.E. Launder, Heat Transfer in Turbulent Mixed Convection, Hemisphere Publishing, New York, NY, 1988.
- [19] H. Nemati, A. Patel, B.J. Boersma, R. Pecnik, The effect of thermal boundary conditions on forced convection heat transfer to fluids at supercritical pressure, J. Fluid Mech. 800 (2016) 531–556.
- [20] N. Zhou, A. Krishnan, Numerical simulation of coupled heat transfer characteristics for flows at supercritical pressure [aircraft fuel flow], in: IECEC 96. Proceedings of the 31st Intersociety Energy Conversion Engineering Conference, vol. 2, IEEE, 1996, pp. 1471–1476.
- [21] L. Wang, Z. Chen, H. Meng, Numerical study of conjugate heat transfer of cryogenic methane in rectangular engine cooling channels at supercritical pressures, Appl. Therm. Eng. 54 (1) (2013) 237–246.

- [22] Z. Zhao, D. Che, Numerical investigation of conjugate heat transfer to supercritical CO2 in a vertical tube-in-tube heat exchanger, Numer. Heat Transf., Part A: Appl. 67 (8) (2015) 857–882.
- [23] Z. Zhao, D. Che, J. Wu, S. Yao, K. Zhang, Y. Lin, H. Ke, Numerical investigation on conjugate cooling heat transfer to supercritical CO2 in vertical double-pipe heat exchangers, Numer. Heat Transf., Part A: Appl. 69 (5) (2016) 512–528.
- [24] K.Y. Chien, Predictions of channel and boundary-layer flows with a low-Reynolds-number turbulence model, AIAA J. 20 (1) (1982) 33–38.
- [25] J.D. Jackson, W.B. Hall, Influences of buoyancy on heat transfer to fluids flowing in vertical tubes under turbulent conditions, Turbul. Forced Convect. Channels Bundles 2 (1979) 613–640.
- [26] K. Abe, T. Kondoh, Y. Nagano, A new turbulence model for predicting fluid flow and heat transfer in separating and reattaching flows—I. Flow field calculations, Int. J. Heat Mass Transfer 37 (1) (1994) 139–151.
- [27] K. Abe, T. Kondoh, Y. Nagano, A new turbulence model for predicting fluid flow and heat transfer in separating and reattaching flows—II. Thermal field calculations. Int. J. Heat Mass Transfer 38 (8) (1995) 1467–1481.
- [28] M. Behnia, S. Parneix, P.A. Durbin, Prediction of heat transfer in an axisymmetric turbulent jet impinging on a flat plate, Int. J. Heat Mass Transfer 41 (12) (1998) 1845–1855.
- [29] Z. Yang, T. Shih, A k ε calculation of transitional boundary layers, in: Instabil., Transition, Turbul., Springer, 1992, pp. 611–620.
- [30] Z. Zhao, D. Che, Y. Zhang, S. Yao, K. Zhang, Y. Lin, Numerical investigation on conjugate heat transfer to supercritical CO2 in membrane helical coiled tube heat exchangers, Numer. Heat Transf., Part A: Appl. 69 (9) (2016) 977–995.
- [31] X. Sun, K. Xu, H. Meng, Y. Zheng, Buoyancy effects on supercritical-pressure conjugate heat transfer of aviation kerosene in horizontal tubes, J. Supercrit. Fluids 139 (2018) 105–113.
- [32] K. Xu, X. Sun, H. Meng, Conjugate heat transfer, endothermic fuel pyrolysis and surface coking of aviation kerosene in ribbed tube at supercritical pressure, Int. J. Therm. Sci. 132 (2018) 209–218.
- [33] F. Luo, Studies on Flow and Heat Transfer Involved in Enhanced Geothermal System and Carbon Dioxide Utilization (Ph.D. thesis), Tsinghua University, 2014.
- [34] M. Seddighi, Study of Turbulence and Wall Shear Stress in Unsteady Flow Over Smooth and Rough Wall Surfaces (Ph.D. thesis), University of Aberdeen, 2011.
- [35] S. He, M. Seddighi, Turbulence in transient channel flow, J. Fluid Mech. 715 (2013) 60–102.
- [36] W. Wang, S. He, Mechanisms of buoyancy effect on heat transfer in a horizontal flow, in: Proceedings of the 7th International Symposium on Supercritical Water-Cooled Reactors, ISSCWR-7, 2015, pp. 15–18.
- [37] C.D. Pierce, Progress-Variable Approach for Large-Eddy Simulation of Turbulent Combustion, Stanford University, 2001.
- [38] E. Lemmon, M. Huber, M. McLinden, NIST standard reference database 23: Reference fluid thermodynamic and transport properties-REFPROP, version 8.0. National institute of standards and technology, standard reference data program, 2018. Standard Reference Data Program. Gaithersburg.
- [39] I. Tiselj, L. Cizelj, DNS of turbulent channel flow with conjugate heat transfer at Prandtl number 0.01, Nucl. Eng. Des. 253 (2012) 153–160.
- [40] J. He, W. Wang, J. Yan, A. Pucciarelli, P. Jiang, W. Ambrosini, S. He, Study of fluid-to-fluid scaling for upward pipe flows of supercritical fluids using direct numerical simulation. Int. J. Heat Mass Transfer 189 (2022) 122651.
- [41] G.K. El Khoury, P. Schlatter, A. Noorani, P.F. Fischer, G. Brethouwer, A.V. Johansson, Direct numerical simulation of turbulent pipe flow at moderately high Reynolds numbers, Flow, Turbul. Combust. 91 (3) (2013) 475–495.
- [42] D.P. DeWitt, F.P. Incropera, T.L. Bergman, A.S. Lavine, Fundamentals of Heat and Mass Transfer, sixth ed., John Wiley, 2007.
- [43] V. Gnielinski, Neue Gleichungen für den Wärme-und den Stoffübergang in turbulent durchströmten Rohren und Kanälen, Forschung im Ingenieurwesen A 41 (1975) 8–16.
- [44] C.F. Colebrook, C.M. White, Experiments with fluid friction in roughened pipes, Proc. R. Soc. London. Ser. A-Math. Phys. Sci. 161 (906) (1937) 367–381.
- [45] J. You, J.Y. Yoo, H. Choi, Direct numerical simulation of heated vertical air flows in fully developed turbulent mixed convection, Int. J. Heat Mass Transfer 46 (9) (2003) 1613–1627.
- [46] S. He, K. He, M. Seddighi, Laminarisation of flow at low Reynolds number due to streamwise body force, J. Fluid Mech. 809 (2016) 31–71.
- [47] K. Fukagata, K. Iwamoto, N. Kasagi, Novel turbulence control strategy for simultaneously achieving friction drag reduction and heat transfer augmentation, in: Fourth International Symposium on Turbulence and Shear Flow Phenomena, Begel House Inc., 2005.
- [48] T. Gomez, V. Flutet, P. Sagaut, Contribution of Reynolds stress distribution to the skin friction in compressible turbulent channel flows, Phys. Rev. E 79 (3) (2009) 035301.